

# Convective heat transport in stratified atmospheres at low and high Mach number

Evan H. Anders and Benjamin P. Brown

Department of Astrophysical & Planetary Sciences, University of Colorado – Boulder and  
Laboratory for Atmospheric and Space Physics, Boulder, CO

Convection in astrophysical systems is stratified and often occurs at high Rayleigh number (Ra) and low Mach number (Ma). Here we study stratified convection in the context of plane-parallel, polytropically stratified atmospheres. We hold the density stratification ( $n_\rho$ ), aspect ratio, and Prandtl number (Pr) constant while varying the superadiabaticity and Ra. We find that Ma is a strong function of the superadiabaticity and a weak function of the Rayleigh number. We also examine the behavior of the Nusselt number (Nu), which quantifies the efficiency of convective heat transport, and the Reynolds number (Re), which quantifies how turbulent our solutions are. Both of these measures experience weaker scaling when the evolved solution has an average Ma of one than they do in the low Ma regime.

## INTRODUCTION

Convection transports energy in stellar and planetary atmospheres. In these objects, flows are compressible and feel the atmospheric stratification. While in some systems this stratification is negligible, it is significant in regions such as the convective envelope of the Sun, which spans 14 density scale heights. In the bulk of these systems, flows are at very low Mach Number (Ma), but numerical constraints have restricted most studies of compressible convection to high Ma. These studies have provided important insight into the low temperature, high Ma region near the Sun’s surface, but few fundamental properties of low Ma convection which characterize deeper motions are known.

In the widely-studied Rayleigh-Bénard (RB) problem of incompressible Boussinesq convection, upflows and downflows are symmetrical, and the conductive flux ( $\propto \nabla T$ ) approaches zero in the convective interior. Early numerical experiments of moderate-to-high Ma compressible convection in two [1–4] and three [5, 6] dimensions revealed that these two hallmark characteristics of RB convection change significantly when stratification is included. Downflow lanes become fast and narrow, and upflow lanes turn into broad, slow upwellings. Furthermore, the *entropy* gradient is negated by convection rather than the temperature gradient, and a significant conductive flux can exist in the presence of efficient convection.

In RB convection, there exist two primary dynamical control parameters: the Rayleigh number (Ra, the ratio of buoyant driving to diffusive damping) and the Prandtl number (Pr, the ratio of viscous to thermal diffusivity). These numbers control two useful measures of turbulence in the evolved solution: the Reynolds number (Re, the strength of advection to viscous diffusion) and the Peclet number (Pe = Re Pr). Stratified atmospheres with negative entropy gradients are unstable to convection. The magnitude of the unstable entropy gradient, or the superadiabaticity, joins Ra and Pr as an important control parameter. This *superadiabatic excess* [1],  $\epsilon$ , which sets the scale of the atmospheric entropy gradient, primarily

controls the Ma of the evolved solution.

In this letter we study the behavior of convective heat transport, quantified by the Nusselt number (Nu), in plane-parallel, two- and three-dimensional, polytropically stratified atmospheres. We vary  $\epsilon$  and Ra while holding Pr, aspect ratio, boundary conditions, and initial atmospheric stratification constant. We also examine the behavior of flow speeds, as quantified by Ma, and the level of turbulence in solutions, as quantified by Re.

## EXPERIMENT

We examine a monatomic ideal gas with an adiabatic index of  $\gamma = 5/3$  whose equation of state is  $P = R\rho T$ . This is consistent with the approach used in earlier work and is the simplest stratified extension of RB. We study atmospheres which are initially polytropically stratified,

$$\begin{aligned}\rho_0(z) &= \rho_t(1 + L_z - z)^m, \\ T_0(z) &= T_t(1 + L_z - z),\end{aligned}\quad (1)$$

where  $m$  is the polytropic index and  $L_z$  is the depth of the atmosphere. The height coordinate,  $z$ , increases upwards in the range  $[0, L_z]$ . We specify the depth of the atmosphere,  $L_z = e^{n_\rho/m} - 1$ , by choosing the number of density scale heights,  $n_\rho$ , it spans. Throughout this letter we set  $n_\rho = 3$ . Satisfying hydrostatic equilibrium sets the value of gravity,  $g = RT_t(m+1)$ , which is constant with depth. We study atmospheres with aspect ratios of 4 where both the  $x$  and  $y$  coordinates have the range  $[0, 4L_z]$ . In our 2D cases, we only consider  $x$  and  $z$ .

Convective dynamics are controlled by the superadiabaticity of the atmospheres as well as the atmospheric diffusivities. The superadiabaticity, or the magnitude of the (negative) entropy gradient, is set by the superadiabatic excess,  $\epsilon = m_{ad} - m$ , where  $m_{ad} = (\gamma - 1)^{-1}$ . The atmospheric thermal diffusivity,  $\chi$ , and kinematic viscosity (or viscous diffusivity),  $\nu$ , are determined by the Rayleigh number (Ra) and the Prandtl number (Pr). We set  $\text{Pr} = \nu/\chi = 1$  throughout this work. The polytropic

initial conditions are in thermal equilibrium,  $\kappa_0 \partial_z T_0 = \text{const}$ , so  $\kappa_0 = \chi \rho_0$  must be constant. To keep  $\text{Pr}$  constant with height, we set  $\chi = \chi_t / \rho_0$  and  $\nu = \nu_t / \rho_0$ . Under these constraints, the diffusivity profiles are specified by choosing  $\text{Ra}$  at the top of the domain,

$$\text{Ra}_{\text{top}} = \frac{gL_z^3(\Delta S_0/c_P)}{\nu_t \chi_t}, \quad (2)$$

where  $\Delta S_0 = \epsilon \ln(L_z + 1)$  is the entropy difference between the top and bottom boundaries and  $c_P = R\gamma(\gamma - 1)^{-1}$  is the specific heat at constant pressure. The profiles of  $\nu$  and  $\chi$  are constant with time, and  $\text{Ra}$  at the bottom of the atmosphere is greater than  $\text{Ra}_{\text{top}}$  by a factor of  $e^{2n\rho}$ . This formulation leaves the thermal conductivity,  $\kappa = \rho\chi$ , and the dynamic viscosity,  $\mu = \rho\chi$ , free to evolve as the density profile changes. Throughout this letter, we will use  $\text{Ra}$  and  $\text{Ra}_{\text{top}}$  interchangeably.

We decompose our thermodynamic variables such that  $T = T_0 + T_1$  and  $\ln \rho = (\ln \rho)_0 + (\ln \rho)_1$ , and the velocity  $\mathbf{u} = u\hat{x} + v\hat{y} + w\hat{z}$  has no background component. In our 2D runs,  $v = 0$ . We evolve the Fully Compressible Navier-Stokes equations,

$$\frac{\partial \ln \rho}{\partial t} + \nabla \cdot \mathbf{u} = -\mathbf{u} \cdot \nabla \ln \rho, \quad (3)$$

$$\frac{\partial \mathbf{u}}{\partial t} + \nabla T - \nu \nabla \cdot \bar{\boldsymbol{\sigma}} - \bar{\boldsymbol{\sigma}} \cdot \nabla \nu = -\mathbf{u} \cdot \nabla \mathbf{u} - T \nabla \ln \rho + \mathbf{g} + \nu \bar{\boldsymbol{\sigma}} \cdot \nabla \ln \rho, \quad (4)$$

$$\begin{aligned} \frac{\partial T}{\partial t} - \frac{1}{c_V} (\chi \nabla^2 T + \nabla T \cdot \nabla \chi) &= \\ &- \mathbf{u} \cdot \nabla T - (\gamma - 1) T \nabla \cdot \mathbf{u} \\ &+ \frac{1}{c_V} (\chi \nabla T \cdot \nabla \ln \rho + \nu [\bar{\boldsymbol{\sigma}} \cdot \nabla] \cdot \mathbf{u}), \end{aligned} \quad (5)$$

with the viscous stress tensor given by

$$\sigma_{ij} \equiv \left( \frac{\partial u_i}{\partial x_j} + \frac{\partial u_j}{\partial x_i} - \frac{2}{3} \delta_{ij} \nabla \cdot \mathbf{u} \right). \quad (6)$$

Taking an inner product of (4) with  $\mathbf{u}$  and adding it to (5) reveals the full energy equation,

$$\frac{\partial}{\partial t} \left( \rho \left[ \frac{|\mathbf{u}|^2}{2} + c_V T + \phi \right] \right) + \nabla \cdot (\mathbf{F}_{\text{conv}} + \mathbf{F}_{\text{cond}}) = 0, \quad (7)$$

where  $\mathbf{F}_{\text{conv}} \equiv \mathbf{F}_{\text{enth}} + \mathbf{F}_{\text{KE}} + \mathbf{F}_{\text{PE}} + \mathbf{F}_{\text{visc}}$  is the convective flux and  $\mathbf{F}_{\text{cond}} = -\kappa \nabla T$  is the conductive flux. The individual contributions to  $\mathbf{F}_{\text{conv}}$  are the enthalpy flux,  $\mathbf{F}_{\text{enth}} \equiv \rho \mathbf{u} (c_V T + P/\rho)$ ; the kinetic energy flux,  $\mathbf{F}_{\text{KE}} \equiv \rho |\mathbf{u}|^2 \mathbf{u}/2$ ; the potential energy flux,  $\mathbf{F}_{\text{PE}} \equiv \rho \mathbf{u} \phi$  (with  $\phi \equiv -gz$ ); and the viscous flux,  $\mathbf{F}_{\text{visc}} \equiv -\rho \nu \mathbf{u} \cdot \bar{\boldsymbol{\sigma}}$ , and each must be considered. Understanding how these fluxes interact is crucial in characterizing convective heat transport.

We utilize the Dedalus<sup>1</sup> [7] pseudospectral framework to time-evolve (3)-(5) using an implicit-explicit (IMEX),

third-order, four-step Runge-Kutta timestepping scheme RK443 [8]. Variables are time-evolved on a dealiased Chebyshev (vertical) and Fourier (horizontal, periodic) domain in which the physical grid dimensions are 3/2 the size of the coefficient grid. Grid sizes range from 64x256 coefficient points at the lowest values of  $\text{Ra}$  to 1024x4096 coefficient points at  $\text{Ra} > 10^7$  in 2D, and from 64x128<sup>2</sup> to 256x512<sup>2</sup> in 3D. By using IMEX timestepping, we implicitly step the stiff linear acoustic wave contribution and are able to efficiently study flows at moderate ( $\approx 1$ ) and very low ( $\approx 10^{-4}$ ) Ma. Our equations take the form of the FC equations in [9], extended to include  $\nu$  and  $\chi$  which vary with depth, and we follow the approach there. This IMEX approach has been successfully tested against a nonlinear benchmark of the compressible Kelvin-Helmholtz instability [10].

We impose impenetrable, stress free, fixed temperature boundary conditions at the top and bottom of the domain such that  $w = \partial_z u = T_1 = 0$  at  $z = \{0, L_z\}$ .  $T_1$  is initially filled with random white noise whose magnitude is infinitesimal compared to  $T_0$  and  $\epsilon$ . We filter this noise spectrum in coefficient space, such that 25% of the coefficients have power. We non-dimensionalize our computational domains by setting all thermodynamic variables to unity at  $z = L_z$  by choosing  $R = T_t = \rho_t = 1$ . By this choice, the non-dimensional grid length scale is the inverse temperature gradient scale and the simulation timescale is the isothermal sound crossing time,  $\tau_I$ , of this unit length. Meaningful convective dynamics occur on timescales of the atmospheric buoyancy time,  $t_b = \tau_I \sqrt{L_z/g\epsilon}$ . All reported results are taken from time averages over many buoyancy times beginning  $100t_b$  after the start of our simulations in order to assure our results are not biased by the convective transient.

## RESULTS

Solutions were time-evolved until a long time average of the fluxes showed little variance with depth. By performing a linear stability analysis, we determined that the onset of convection in 2D occurs at  $\text{Ra}_{\text{crit}} = \{11.15, 10.06, 10.97, 10.97\}$  for  $\epsilon = \{1.0, 0.5, 10^{-4}, 10^{-7}\}$ , respectively. These onset values hold in 3D. We studied Rayleigh numbers  $\lesssim \{10^7, 10^5, 10^4, 10^3\} \text{Ra}_{\text{crit}}$  for  $\epsilon = \{0.5, 10^{-4}, 1.0, 10^{-7}\}$ , respectively.

We find that the Mach number is a strong function of  $\epsilon$  and a weak function of  $\text{Ra}$ . When  $\text{Ma} < 1$ , we observe a scaling law of  $\text{Ma}(\text{Ra}, \epsilon) \propto \epsilon^{1/2} \text{Ra}^{1/4}$ , but this relation breaks down as the mean Ma approaches 1 and the flows become supersonic (see Fig. 1). Furthermore, the value of  $\epsilon$  sets the size of the evolved thermodynamic variables, such that  $T_1/T_0 \propto \epsilon$  and  $\rho_1/\rho_0 \propto \epsilon$ . These fluctuations are very small when  $\epsilon$  and Ma are small, but can be O(1) for values of  $\epsilon$  near  $m_{\text{ad}}$ .

Low Ma flows (e.g.  $\epsilon = 10^{-4}$ ) display the classic nar-

<sup>1</sup> <http://dedalus-project.org/>

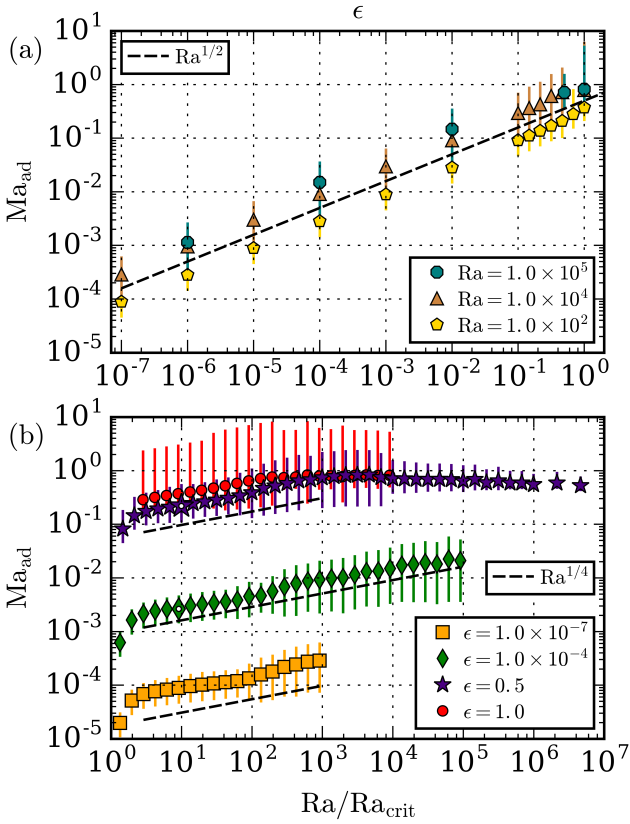


FIG. 1. The mean adiabatic Mach number of long-time-averaged profiles is shown. Error bars show the full range of Ma over the depth of the atmosphere. (a) Ma is plotted as a function of  $\epsilon$ , the superadiabatic excess, at various values of Ra. (b) Ma is plotted as a function of Ra at various values of  $\epsilon$ . Larger symbols with white dots designate 3D runs.

row downflow and broad upflow lanes of stratified convection (Fig. 2a). While it has been suggested that buoyancy breaking as a result of pressure forces leads to the asymmetric nature of up- and downflows [3], at low  $\epsilon$  this effect seems to be unimportant, and the convective structures form as a result of flows obeying mass conservation while traversing the stratified medium. Our choice of fixed-temperature, stress free boundary conditions allows the flux at the boundaries to vary, while also allowing for domain-wide horizontal velocity profiles along the boundaries. 2D runs at  $\text{Ra} > 10^3 \text{Ra}_{\text{crit}}$  and  $\epsilon = 10^{-4}$  exhibit long-term states of flux disequilibrium, in which roll solutions such as those pictured in Fig. 2a are punctuated by shearing states similar to those previously reported in two-dimensional RB convection [11]. During both of these states, the system is in flux disequilibrium. A long time average over both of these states produces a flat flux profile which can be sensibly analyzed, but the presence of these time-dependent states makes it difficult to measure fluid quantities in these higher-Ra cases at low  $\epsilon$ .

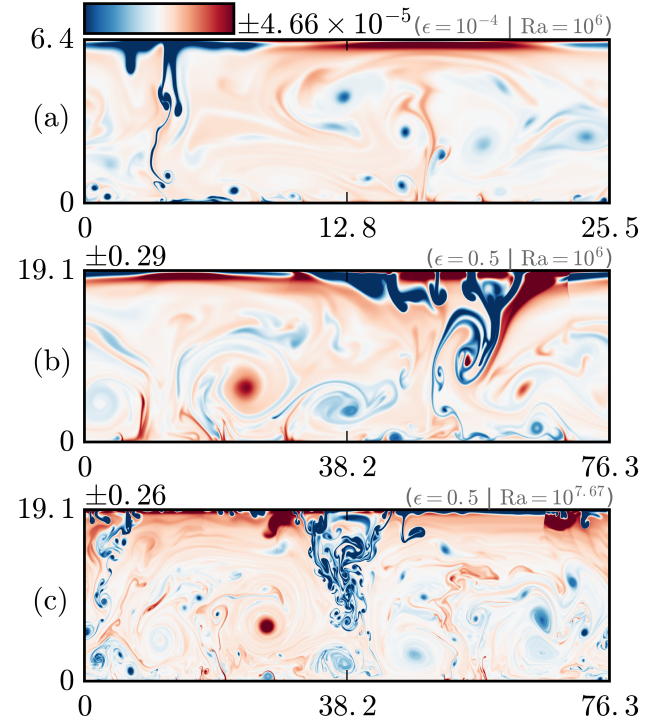


FIG. 2. Characteristic entropy fluctuations in evolved flows roughly  $140t_b$  after the start of simulations. The time- and horizontally-averaged profile is removed in all cases. (a) An  $\epsilon = 10^{-4}$ , low Ma flow. (b) An  $\epsilon = 0.5$ , flow, in which shock systems can be seen in the upper atmosphere (e.g.  $(x, z) \approx (30, 18 - 19), (70, 15 - 19)$ ). (c) A high Ra,  $\epsilon = 0.5$  case. Convective structures become much smaller scale, and shock systems can be seen near  $(x, z) \approx (30, 16 - 19), (65, 17 - 19)$ .

At high Ma (e.g.  $\epsilon = 0.5$ ), bulk thermodynamic structures are similar but shock systems form in the upper atmosphere near downflow lanes for sufficiently large values of  $\epsilon$  and Ra (Fig. 2b,c). Similar shock phenomena were reported in both two [4] and three [12] dimensional polytropic simulations previously. As Ra is increased to large values (Fig. 2c), thermodynamic structures no longer span the whole domain but rather break up into small eddies which traverse the domain multiple times before diffusing.

The efficiency of convection is quantified by the Nusselt number (Nu). Nu is well-defined in RB convection as the total flux normalized by the steady-state conductive flux [13, 14]. In stratified convection Nu is more difficult to define, and we use a modified version of a traditional stratified Nusselt number [1, 3],

$$\text{Nu} \equiv \frac{\langle F_{\text{conv},z} + F_{\text{cond},z} - F_A \rangle}{\langle F_{\text{cond},z} - F_A \rangle} = 1 + \frac{\langle F_{\text{conv},z} \rangle}{\langle F_{\text{cond},z} - F_A \rangle} \quad (8)$$

where  $F_{\text{conv},z}$  and  $F_{\text{cond},z}$  are the z-components of  $\mathbf{F}_{\text{conv}}$  and  $\mathbf{F}_{\text{cond}}$ , and  $\langle \rangle$  are volume averages.  $F_A \equiv -\langle \kappa \rangle \partial_z T_{\text{ad}}$  is the conductive flux of the proper corresponding adia-

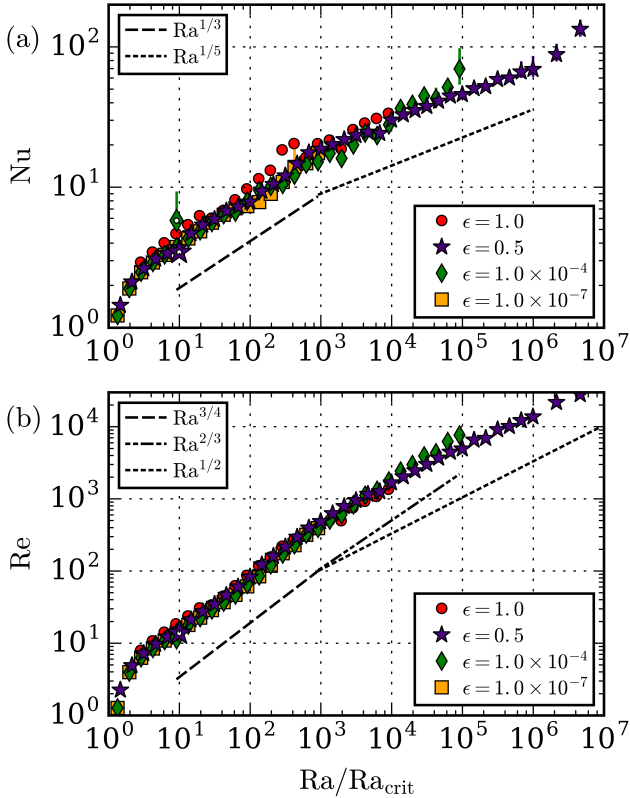


FIG. 3. (a) Variation of  $Nu$  as  $Ra$  increases at high and low  $\epsilon$ . Errors bars indicate the properly normalized range of the value of  $Nu$  as a function of depth and large error bars indicate a poorly converged solution. (b) Variation of  $Re$  as  $Ra$  increases at high and low  $\epsilon$ .  $Re$  is measured at the midplane of the atmosphere. Larger symbols with white dots designate 3D runs. .

batic atmosphere in thermal equilibrium. For a compressible ideal gas in hydrostatic equilibrium,  $\partial_z T_{\text{ad}} \equiv -g/c_P$  [15]. It is important to measure the evolved value of  $\langle \kappa \rangle = \langle \rho \chi \rangle$ , which is nearly  $\kappa_0$  when  $\epsilon$  is small but can change appreciably for large values of  $\epsilon$ . In incompressible Boussinesq convection, where  $\nabla S = 0$  only when  $\nabla T = 0$ , this definition reduces to the traditional definition of the Nusselt number [13, 14].

The variation of  $Nu$  with  $Ra$  is shown in Fig. 3a. At low to moderate  $Ra$ ,  $Nu \propto Ra^{1/3}$  regardless of  $\epsilon$ , reminiscent of scaling laws in classical Rayleigh-Bénard theory [16]. At large  $Ra$ ,  $Nu \propto Ra^{1/5}$  at  $\epsilon = 0.5$ . The scaling of  $Nu$  with  $Ra$  is unclear at low  $\epsilon$  once  $Ra$  is sufficiently large for shearing states to occur. It is also important to note that the value of  $Nu$  is heavily dependent upon the specific thermodynamic structures of the solution, as double roll states will transport heat more efficiently than single roll states, and slight changes in  $Ra$  can result in a solution latching on to one solution or the other.

The Reynolds number ( $Re = |\mathbf{u}|L_z/\nu$ ) and Peclet number ( $Pe = \text{Pr} Re$ ) compare the importance of advection

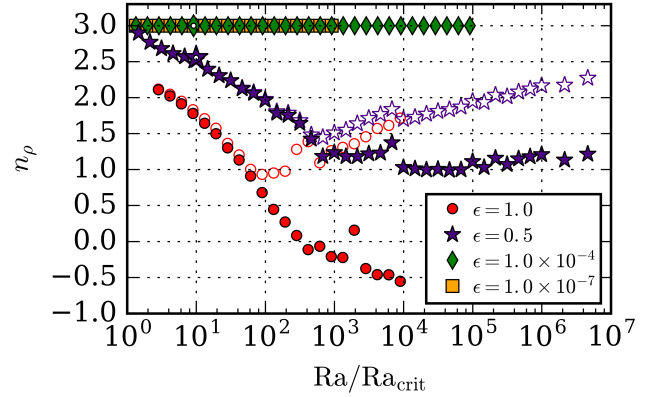


FIG. 4. The stratification of evolved solutions is measured in two ways. Solid symbols show  $\ln(\rho(z=0)/\rho(z=L_z))$ , the density contrast as measured at the upper and lower boundary. The empty symbols show  $\ln(\max(\rho)/\min(\rho))$ . Unsurprisingly, at low  $\epsilon$  the evolved  $n_\rho$  is not different from the initial conditions to first order. At high  $\epsilon$ , the density contrast shrinks, and once the mean Ma approaches 1 (as in Fig. 1b), the two methods of measuring the density stratification bifurcate as density inversions form within the thermal boundary layers. Larger symbols with white dots represent 3D runs.

to diffusion in the evolved convective state. For  $\text{Pr} = 1$ , such as in this work,  $\text{Pe} = \text{Re}$ . Our choice of  $\{\nu, \chi\} \propto \rho_0^{-1}$  drastically changes the value of  $\text{Re}$  between the top and bottom of the atmosphere. We report values of  $\text{Re}$  at the midplane ( $z = L_z/2$ ) of the atmosphere in Fig. 3b. At low  $Ra$ ,  $\text{Re} \propto Ra^{3/4}$ . At high  $Ra$  and  $\epsilon$ , where the average  $\text{Ma} \approx 1$ , this scaling gives way to a  $\text{Re} \propto Ra^{1/2}$ , where all changes in  $\text{Re}$  are due to the lowering of the diffusivity through raising  $Ra$ . For large values of  $Ra$  but at low  $\epsilon$ , there appears to be a scaling of  $\text{Re} \propto Ra^{2/3}$ , but once again the shearing states have made these points difficult to measure.

As the thermodynamic variables converge to their steady state values, the density profile evolves while remaining in hydrostatic equilibrium to zeroth order. In Fig. 4 we show the number of density scale heights present in the evolved solution using two measures. We find that once the average  $\text{Ma}$  of the domain becomes approximately one, large density inversions begin to form in the boundary layers, as was reported by [17]. The agreement of  $Nu$  across  $\epsilon$  (Fig. 3a), particularly at low  $Ra$  in which all four of our cases collapse onto a single power law, is striking in light of the vastly different evolved stratifications felt by the flows.

## DISCUSSION

In this letter we have studied fundamental heat transport by stratified convection in simplified 2D and 3D polytropic atmospheres. We argue that these atmo-

spheres are the natural extension of the RB problem to stratified systems, and are an ideal laboratory for understanding the basic properties of stratified convection. We see little difference between the properties of our 2D and 3D results, which aligns with expectations of Boussinesq theory and numerical simulation results at values of  $\text{Pr} \geq 1$  [18].

At low Ra and Ma, the scaling of Nu with Ra is reminiscent of RB convection. However, at high Ra and Ma, the scaling of Nu becomes weaker, changing from a  $1/3$  to a  $1/5$  power law, a decrease by nearly a factor of  $1/3$ . Similarly, the Reynolds number switches from a  $3/4$  power law to a  $1/2$  scaling in this regime shift, a similar decrease. This seems to suggest that a large portion of the scaling of the Nusselt number and Reynolds number in the low-Ma regime comes from increases in velocity. Once the velocity reaches its natural maximum, heat transport can no longer benefit from increased velocities. The same is true of the Reynolds number, which scales directly with system diffusivities once the Mach number reaches its maximum value.

Time-dependent oscillating shear states have developed spontaneously at values of  $\epsilon = 10^{-4}$  and  $\text{Ra} \gtrsim 10^3 \text{Ra}_{\text{crit}}$  in our 2D simulations. Similar states have been observed in 2D RB convection [11], and these should be studied in more detail. These states are fundamentally in flux disequilibrium and last for large time scales ( $O(100t_b)$ ), making it very difficult to choose a proper time window over which to calculate a meaningful Nusselt number. It would be beneficial for future studies to examine atmospheres with fixed flux or no slip boundary conditions to better converge and study cases at low  $\epsilon$  and high Ra.

Finally, we have found that the stratification of these atmospheres evolves in a complex manner. Future work should aim to understand the importance of stratification on convective heat transport, and the manner in which boundary layer density inversions interact with the formation and transport properties of thermal plumes.

Our studies here will serve as a foundation both for understanding and comparing heat transport in stratified convection to that in RB convection [13], and for future studies of transport in stratified convection. These results can be used to determine if simplified equation sets, such as the anelastic equations, carry heat in the same manner as the FC equations. This work will also be useful in coming to understand more realistic systems, such as rapidly rotating atmospheres [19], atmospheres bounded by stable regions [20], or regions with realistic profiles of  $\kappa$ .

#### acknowledgements

EHA acknowledges the support of the University of Colorado's George Ellery Hale Graduate Student Fellow-

ship. This work was additionally supported by NASA LWS grant number NNX16AC92G. Computations were conducted with support by the NASA High End Computing (HEC) Program through the NASA Advanced Supercomputing (NAS) Division at Ames Research Center on Pleiades with allocations GID s1647 and GID g26133. We thank Jon Aurnou, Axel Brandenburg, Keith Julien, Mark Rast, and Jeff Oishi for many useful discussions. We also thank the two anonymous referees whose critical comments greatly improved the quality of this letter.

- 
- [1] E. Graham, Journal of Fluid Mechanics **70**, 689 (1975).
  - [2] K. L. Chan, S. Sofia, and C. L. Wolff, Astrophys. J. **263**, 935 (1982).
  - [3] N. E. Hurlburt, J. Toomre, and J. M. Massaguer, Astrophys. J. **282**, 557 (1984).
  - [4] F. Cattaneo, N. E. Hurlburt, and J. Toomre, ApJL **349**, L63 (1990).
  - [5] F. Cattaneo, N. H. Brummell, J. Toomre, A. Malagoli, and N. E. Hurlburt, Astrophys. J. **370**, 282 (1991).
  - [6] N. H. Brummell, N. E. Hurlburt, and J. Toomre, Astrophys. J. **473**, 494 (1996).
  - [7] K. Burns, G. Vasil, D. Lecoanet, J. Oishi, and B. Brown, *Dedalus: Flexible framework for spectrally solving differential equations*, Astrophysics Source Code Library (2016), 1603.015.
  - [8] U. M. Ascher, S. J. Ruuth, and R. J. Spiteri, Applied Numerical Mathematics **25**, 151 (1997).
  - [9] D. Lecoanet, B. P. Brown, E. G. Zweibel, K. J. Burns, J. S. Oishi, and G. M. Vasil, Ap. J. **797**, 94 (2014), 1410.5424.
  - [10] D. Lecoanet, M. McCourt, E. Quataert, K. J. Burns, G. M. Vasil, J. S. Oishi, B. P. Brown, J. M. Stone, and R. M. O'Leary, MNRAS **455**, 4274 (2016), 1509.03630.
  - [11] D. Goluskin, H. Johnston, G. R. Flierl, and E. A. Spiegel, Journal of Fluid Mechanics **759**, 360 (2014).
  - [12] A. Malagoli, F. Cattaneo, and N. H. Brummell, ApJL **361**, L33 (1990).
  - [13] H. Johnston and C. R. Doering, Physical Review Letters **102**, 064501 (2009), 0811.0401.
  - [14] J. Otero, R. W. Wittenberg, R. A. Worthing, and C. R. Doering, Journal of Fluid Mechanics **473**, 191 (2002).
  - [15] E. A. Spiegel and G. Veronis, Astrophys. J. **131**, 442 (1960).
  - [16] E. M. King, S. Stellmach, and J. M. Aurnou, Journal of Fluid Mechanics **691**, 568 (2012).
  - [17] A. Brandenburg, K. L. Chan, Å. Nordlund, and R. F. Stein, Astronomische Nachrichten **326**, 681 (2005), astro-ph/0508404.
  - [18] G. Ahlers, S. Grossmann, and D. Lohse, Rev. Mod. Phys. **81**, 503 (2009).
  - [19] K. Julien, E. Knobloch, A. M. Rubio, and G. M. Vasil, Physical Review Letters **109**, 254503 (2012).
  - [20] N. E. Hurlburt, J. Toomre, and J. M. Massaguer, Astrophys. J. **311**, 563 (1986).